Spectrochimica Acta Part A: Molecular and Biomolecular Spectroscopy 345 (2026) 126772

Contents lists available at ScienceDirect

Spectrochimica Acta Part A:
Molecular and Biomolecular Spectroscopy

journal homepage: www.journals.elsevier.com/spectrochimica-acta-part-a-molecular-and-biomolecular-spectroscopy

Acrylamide molecule detection by surface-enhanced infrared absorption spectroscopy using resonant nanoantennas

Santos Merino [a,b,*], Alberto Villar [a], Ruth Díez-Ahedo [a], Eider Gárate [c], Iban Amenabar [d], Ralph Gay [d], Jorge Espina [e], Mario Zapata-Herrera [f], Roberto A. Boto [f], Javier Aizpurua [b,f,g]

[a] Surface Chemistry and Nanotechnologies Unit, Tekniker, Eibar 20600, Spain
[b] Departamento de Electricidad y Electrónica, Universidad del País Vasco UPV/EHU, 48940 Leioa, Spain
[c] Intelligent Information Systems Unit, Tekniker, Eibar 20600, Spain
[d] CIC nanoGUNE BRTA, Tolosa Hiribidea 76, 20018 San Sebastián, Spain
[e] Servicios Científico-Técnicos, Universidad de Oviedo, C/Fernando Bongera s/n, 33006, Oviedo, Spain
[f] Donostia International Physics Center, Paseo Manuel Lardizabal 4, 20018, Donostia-San Sebastián, Spain
[g] Ikerbasque, Basque Foundation for Science, 48009, Bilbao, Spain

HIGHLIGHTS

- DFT was used to study the IR absorption of acrylamide in the presence of a gold cluster to identify target vibrational modes.
- Gold nanoantennas were designed and fabricated to resonate with target vibrational modes.
- Strong coupling and Fano resonances arise from interactions between acrylamide vibrations and gold nanoantenna plasmons.
- SEIRA spectroscopy can detect acrylamide concentrations as low as 500 ng/ml in aqueous solutions.

GRAPHICAL ABSTRACT

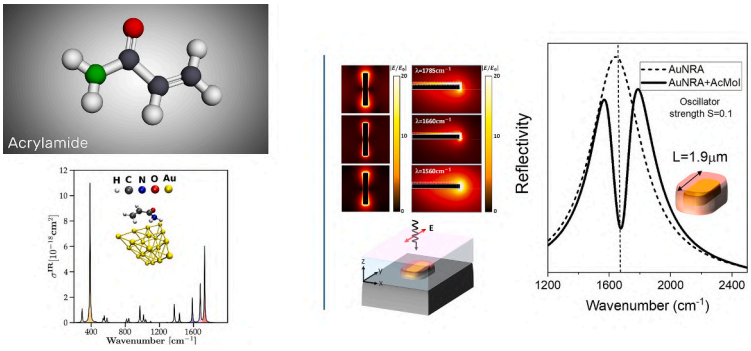

ARTICLE INFO

Keywords:
Plasmonic nanoantennas
Density functional theory (DFT)
Surface-enhanced infrared absorption spectroscopy (SEIRA)
Acrylamide

ABSTRACT

Acrylamide is a cancer-causing substance that forms in food by Maillard reaction when free asparagine (an amino acid) and sugars, both naturally present, undergo high-temperature processing (>120 °C) and low humidity conditions. The European Food Safety Authority (EFSA) has identified acrylamide as a significant contaminant that needs to be monitored and minimized in certain food products. This work reports the first step to detect the presence of acrylamide in aqueous solution by Surface-Enhanced Infrared Absorption (SEIRA) spectroscopy. This work applies Density Functional Theory (DFT) to calculate the vibrational frequencies and infrared (IR) absorption cross-sections of molecular acrylamide in close proximity to gold nanoantenna arrays in water-based solutions. These IR nanoantennas are designed through electromagnetic calculations of their electromagnetic response by tunning their plasmon resonance to match the characteristic vibrational frequencies of acrylamide, enhancing the molecular spectroscopic signal. Comprehensive characterization of the SEIRA signal for various gold nanorod antennas (AuNRA) coupled with a covering shell containing molecular acrylamide enables direct

* Corresponding author at: Surface Chemistry and Nanotechnologies Unit, Tekniker, Eibar 20600, Spain.
E-mail address: santos.merino@tekniker.es (S. Merino).

https://doi.org/10.1016/j.saa.2025.126772
Received 6 June 2025; Received in revised form 24 July 2025; Accepted 31 July 2025
Available online 5 August 2025

identification of its vibrational modes. This work shows how concentrations of up to 500 ng/ml of acrylamide in water can be detected by SEIRA. It also provides guidelines to apply SEIRA for the detection of acrylamide in challenging samples, such as those typically found in the food industry.

1. Introduction

Acrylamide is a molecule that naturally forms from asparagine by the Maillard reaction in starchy food products during a high-temperature process (including frying, baking, roasting and industrial processing) at +120 °C and low moisture conditions and under the presence of sugars (e.g. glucose, fructose, among others) in food. It is found in products such as potato crisps, French fries, bread, biscuits and coffee. This molecule potentially increases the risk of developing cancer for consumers in all age groups as declared by the EFSA (European Food Safety Authority) in 2015 [1] and revised later in 2022 [2]. In parallel to this statement, the European Commission established [3] mitigation measures and benchmark levels for the reduction of the presence of acrylamide in food. Despite these measures, there are still a severe lack of data for highly consumed foods that might contain significant levels of acrylamide. Thus the European Commission recommended [4] to the ruling authorities and food business operators to monitor the presence of acrylamide in such food following the adoption of possible risk management measures.

So far, some methods have been used to quantify acrylamide in foodstuffs. Most of them suffer significantly from high instrument costs and complex operations, such as high-performance liquid chromatography (HPLC). Alternatively, immunoassays based on the specificity of an antibody to recognize acrylamide have been reported [5]. As acrylamide alone is too small to elicit an immune response, it is converted into an immunogenic derivative, which enables the production of specific antibodies and its use alongside polyclonal antibodies in immunoassays such as ELISA [6], electrochemical immunosensor [7] or fluorescent immunoassays [8]. However, traditional antibodies present certain limitations. For example, polyclonal antibodies often suffer from inconsistent quality due to batch-to-batch variability among immunized animals. Additionally, monoclonal antibodies can lose specificity after thawing hybridoma cells, as these may begin expressing additional functional variable regions. To solve partially this limitation, nanobodies were introduced because they do not rely on hybridomas, which are prone to genetic instability and can be produced from bacteria, yeast or stable cell cultures. However, the functionality and signal of the nanobody can be affected by the chemical functionalization required to bind the nanobody to the surface.

Infrared (IR) absorption spectroscopy is a powerful method that provides valuable information for molecular recognition. Infrared light can excite molecular vibrations, which are characterized by dipole moment oscillations at the frequency of incoming light. The absorption frequencies serve as molecular fingerprints, enabling the identification of molecules without the need for neither label molecules nor specific receptors. Infrared absorption spectroscopy is a remarkable analytical technique offering excellent specificity for target molecules, though it has moderate sensitivity compared to immunoassays-based analytical methods. This is mainly due to the fact that molecules typically exhibit small IR absorption cross-sections, which results in a limited sensitivity. To increase the sensitivity of the absorption process, nanometer-sized antennas of different materials are commonly used, which enhance the characteristic IR absorption of the target molecules due to the electromagnetic response of the antenna. This approach is known as Surface-Enhanced Infrared Absorption (SEIRA) spectroscopy [9,10]. The collective oscillations of the surface charge density driven by the free electron gas of the nanoantennas, known as surface plasmons, produce a characteristic response at a given frequency, creating intense local electromagnetic fields around the nanoantenna at specific resonant frequencies. Under resonant conditions, the interaction between these intense fields and the vibrational modes of molecules located in the vicinity of the antenna results in a significant enhancement of the molecular IR absorption cross-section, which can be measured through optical reflectivity. SEIRA has been successfully applied to biomolecular, chemical and gas sensing using plasmonic excitations in metallic nanoparticles, graphene and high-Q resonant dielectric nanoresonators [11].

This work addresses the detection of molecular acrylamide using SEIRA. To optimize the detection sensitivity, the IR absorption spectra of the acrylamide molecule was calculated using Density Functional Theory (DFT), characterizing the vibrational frequencies and their respective IR absorption cross-sections. Furthermore, full electrodynamical calculations were developed to design gold-nanorod antennas with a resonant plasmonic response, which coincides with the molecular bands obtained in the DFT calculations. Thus, different arrays of gold nanoresonators were arranged on a single wafer substrate in which each array was designed for sensitive IR identification of different acrylamide vibrational frequencies. This work demonstrates that gold nanorod antennas can efficiently detect acrylamide concentrations as low as 500 ng/ml in water-based solutions.

2. Materials and methods

2.1. Materials and reagents

Acrylamide molecule (CAS-no. 79–06-1) was purchased from Chem Service (USA) and received with a purity of 99.5 %. Deuterium Oxide (CAS-no. 7789-20-0) of 99.8 % purity was purchased from Scharlab (Spain) and deuterium oxide of 99.95 % purity was purchased from ThermoFisher Scientific and received in Acroseal packaging to reduce the moisture uptake of the solvent. Acrylamide concentrations of 400 ng/ml, 500 ng/ml, 750 ng/ml, 1 μg/ml, 10 μg/ml and 100 μg/ml were prepared in both deuterium oxides solvents.

Calcium Fluoride (CaF_2) wafers were purchased to Redoxme AB (Sweden). For the microfluidic cell fabrication, pressure-sensitive adhesive thin film ARsealTM 90,880 (Adhesive research), polycarbonate Lexan 8010 MC (Konig), Stand-alone female mini luer 10,000,701 (ChipShop), Male mini luer plug 10,000,030 (ChipShop), and double side adhesive tape 3M™ 9088–200 were used.

2.2. Infrared absorption: theoretical study

2.2.1. IR absorption spectra of the pristine molecule

To simulate the IR absorption spectra of acrylamide in water, two sets of DFT calculations were carried out. First, the minimum energy structure of acrylamide in water was computed within the formalism of Density Functional Theory (DFT) using the exchange-correlation functional B3LYP [12], which exhibits a good performance for fundamental vibrational frequencies [13–15] and the basis set def2-SVP [16]. To account for the effect of the solvent on the chemical and electronic structure of acrylamide, the polarizable continuum model (PCM) [17] with water as a solvent was used. Then, the vibrational frequencies and the IR integrated absorption coefficients for all the vibrational modes were obtained using the same exchange-correlation functional, basis set, and solvent model that used for the computation of the minimum energy structure.

2.2.2. Enhancement effects in the IR absorption signal

In order to include the effect of the binding of the molecule to the nanoantenna, to be used later in the full SEIRA calculations, a chemical

model consisting of the acrylamide molecule and a tetrahedral gold cluster of 20 atoms was implemented. First, the molecular structure of acrylamide in water in the presence of the gold cluster was optimized within DFT using the exchange-correlation functional B3LYP and the basis def2-SVP for the atoms of hydrogen, carbon, nitrogen and oxygen. For the atoms of gold of the cluster, the basis set LANL2DZ [18] was used. During the optimization process, the positions of the atoms of the cluster were fixed. To account for the non-covalent interactions between the acrylamide molecule and the gold cluster the empirical dispersion correction D3 of Grimme [19] with the damping function of Becke and Johnson [20] was used. With the aim to include the effect of the solvent on the chemical and electronic structure of acrylamide, the polarizable continuum model with water as a solvent was used. Then, the vibrational frequencies, and the IR integrated absorption coefficient for all the vibrational modes were obtained using the same exchange-correlation functional, basis set and solvent model, as used for the computation of the minimum energy structure. To isolate the vibrational modes of acrylamide from those vibrational modes delocalized between acrylamide and the gold cluster, the positions of the atoms of the cluster were fixed during the computation of the vibrational properties. All the DFT calculations carried out were performed with the code Gaussian 16 [21].

To obtain the IR absorption of the pristine and cluster-attached molecules, the corresponding cross-sections are plotted as a function of the vibrational wavenumber (in cm^{-1}). The IR absorption cross-sections were obtained after averaging over random orientations of the molecule the derivative of the dipole moment with respect to the normal modes coordinates. Then, the calculated cross-sections were fitted to a Lorentzian function of full width at half maximum of 8 cm^{-1}.

2.3. Numerical electromagnetic simulation

To investigate the optical response of the nanoantennas producing the SEIRA effect, Maxwell's equations were solved using the Finite Element Method (FEM), as implemented in the commercial software COMSOL Multiphysics [22]. The lumped port formulation was used and periodic (Floquet) boundary conditions imposed at the in-plane directions of a squared unit cell (x- and y-axes, according to Fig. S1), as well as scattering boundary conditions in the out-of-plane direction (z-axis) as described in Section 1 of the Supplementary Information.

2.4. Micro and nanofabrication

Arrays, each measuring 1 × 1 mm and containing gold nanorod antennas arranged in a square symmetry with a lattice parameter of W = 2.8 μm, were fabricated on a 1" CaF_2 substrate. These arrays consisted of identical gold nanorod antennas (AuNRAs) with lengths (L) of 1.8 μm, 2.1 μm, and 2.4 μm and a width of 300 nm. The arrays were patterned on a CaF_2 wafer (Fig. S2a) using electron beam lithography on a double PMMA layer, followed by gold evaporation (70 nm) and metal lift-off. Cross alignment marks were included on the horizontal axis near the edge of the 1 × 1 mm AuNRAs. These were primarily used for posterior control of incident light polarization along the nanoantenna axis.

The 1 × 1 mm arrays were fabricated on CaF_2 substrates by the following methodology. The substrates were first cleaned with acetone and isopropanol in ultrasounds, and subsequent oxygen plasma for 5 min. After that, a double layer of positive PMMA resist was then spin coated on them. Firstly, a PMMA 495 A4 was spin coated (60 s at 2500 rpm speed) and baked for 5 min at 180 °C and then a second layer of PMMA 950 A2 was spin coated (60 s at 4000 rpm speed) and again baked for 5 min at 180 °C. A layer of gold of 3 nm was sputtered to make the CaF_2 substrates conductive and direct electron beam writing of the antennas (Raith-150, Germany) was then performed. After electron writing, first the top gold layer was removed using a gold etchant and then the PMMA was developed at MIBK/IPA for 40 s. After development, the samples were cleaned by applying oxygen plasma for 5 min and then a 70 nm Au film and a 5 nm Ti underlayer for better adhesion were deposited by thermal and electron beam evaporation, respectively. Finally, the resist was removed by a lift-off process in acetone overnight.

2.5. Microfluidic cell fabrication

A low-cost disposable microfluidic chamber (Fig. S2b) was fabricated for medium-infrared absorption measurements to guarantee a complete wetting and equal amount of sample over the antennas' arrays avoiding liquid evaporation. The chamber was designed to encapsulate the 1" CaF_2 substrate containing arrays of gold nanorods, following the protocol outlined below. Briefly, an 80 μm thick double-sided pressure-sensitive adhesive (PSA) film was pre-cut to match the cell dimensions, with a designated 1.5 cm × 0.5 cm area to define the chamber's boundaries. Finally, to close the chamber a polycarbonate (PC) film containing a precut inlet and outlet was adhered on the top of PSA. Inlet/outlet connectors can be used to facilitate the sample introduction and extraction and they can be sealed after pipetting the sample with scotch tape or plugs to avoid evaporation or sample loss. 15 min after pipetting the sample, the assembled cell was flipped and placed for infrared spectroscopy measurements in inverse reflection geometry.

2.6. SEIRA spectroscopy

SEIRA signals were studied by Fourier-transform infrared (FTIR) spectroscopy using a Varian 620-IR FTIR microscope coupled to a Varian 670-IR spectrometer, equipped with a liquid nitrogen-cooled mercury cadmium telluride detector and referenced to a gold mirror. All SEIRA measurements were performed in reflection mode with an Agilent objective (Numerical Aperture = 0.81) with a Field of Vision of 420 × 420 μm illuminating the chips from the backside (Fig. S3). The measurements were performed at a resolution of 4.0 cm^{-1}, with at least 128 scans averaged per sample. Polarization of the infrared radiation was controlled by employing a rotatable Pike 723–2101 polarizer, which was aligned along the long axis of the gold nanorods.

2.7. Data analysis

Extraction of the acrylamide IR fingerprints is performed by normalizing the reflectance spectrum (%R) of the acrylamide to that of the deuterium oxide in the absence of the molecule, R_0. The differential absorbance spectrum is calculated by subtracting a polynomial baseline fitted by least-squares method to the normalized reflectance [23]. The noise levels are calculated using negative controls, i.e. from three times the absorbance signal generated by the injection of acrylamide-devoid heavy water solution. All error bars represent the standard deviation from two measurements.

3. Results and discussion

3.1. Selection of the target acrylamide IR frequencies

The IR absorption spectrum of acrylamide in solution has been previously addressed [24,25], but the impact of metallic nanostructures on the vibrational properties of acrylamide is not yet fully understood. SEIRA spectra of polyacrylamide adsorbed on gold nanoparticles have been reported and have revealed spectral changes in the vibrational properties of acrylamide [26]. Here, the IR absorption of acrylamide in the presence of a single gold cluster is addressed to select the target vibrational modes that will match the resonances of the gold nanorod antennas.

In SEIRA measurements, the molecule interacts with metallic nanostructures which modify the molecular IR absorption signal due to electromagnetic and chemical interactions between the molecule and the nanostructure. To compute the SEIRA signal of acrylamide, a chemical model is first used to capture the modification of the

absorption cross-section of a single molecule upon binding to metallic atoms. To capture this effect, a system comprising the molecule and a single gold cluster containing 20 atoms in water is considered (Au_{20}-acrylamide). This cluster simulates the chemical environment of the molecule in SEIRA measurements.

Fig. 1 shows the simulated IR absorption spectrum of Au_{20}-acrylamide in water. The IR signal of Au_{20}-acrylamide is characterized by four intense peaks at 1730 cm^{-1}, 1679 cm^{-1}, 1587 cm^{-1} and 387 cm^{-1}.

In the high-frequency region (above 1000 cm^{-1}), the spectrum is dominated by the signal at 1730 cm^{-1}. This signal corresponds to the characteristic stretching mode associated with the chemical bond between the carbon and the oxygen atom (Fig. 1f). In the same frequency range, but with lower intensity, two peaks at 1679 cm^{-1} and 1587 cm^{-1} are observed, which correspond to the C═C stretching mode (Fig. 1e) and to the in-plane symmetric bending motion (scissoring modes) of the hydrogen atoms bonded to the nitrogen (Fig. 1d), respectively. In the low-frequency spectral region (below 1000 cm^{-1}), the most relevant feature of the IR spectrum is the peak at 387 cm^{-1}. The vibrational mode associated with this peak is characterized by the out-of-plane symmetric bending motion (wagging modes) of the hydrogen atoms bonded to the nitrogen atom (Fig. 1b).

The presence of the gold cluster introduces some moderate spectral changes due to the interaction between the molecule and the cluster, as well as the modification of the molecular conformation of acrylamide (see Section S3 of the SI for a discussion on the cluster-molecule interaction). In the most stable configuration of the Au_{20}-acrylamide complex, the molecule adopts a *skew* conformation with the terminal nitrogen and carbon atoms facing each other (compare the insets of Fig. 1a and Fig. S4a) [27]. For instance, the C═C stretching mode, which exhibits a weak intensity peak for the bare molecule (Fig. S4a, e), emerges with strong intensity in the spectrum of Au_{20}-acrylamide (Fig. 1a, e). The scissoring mode of the hydrogen atoms bonded to the carbon atom (Fig. 1c) is also affected by the molecule-cluster interaction. This mode, which is dominant for the bare molecule (Fig. S4a, c), shows very weak intensity for Au_{20}-acrylamide.

IR antennas typically work at spectral frequencies above 1000 cm^{-1}. Therefore, the vibrational modes at 1730 cm^{-1}, 1679 cm^{-1} and 1587 cm^{-1} are selected for further detection with the gold nanorod antennas.

3.2. Theoretical design of gold nanorod antennas coupled to infrared acrylamide frequencies

The design of a platform for detecting the molecular vibrational fingerprints generated by the interaction of acrylamide molecules with arrays of gold nanorod antennas is described in the following. To easily recognize the vibrational fingerprints of acrylamide, this design is aimed at a strong resonance of the gold nanorods in the region of the most intense Au_{20}-acrylamide peaks above 1000 cm^{-1}, specifically located at 1730 cm^{-1}, 1679 cm^{-1}, and 1587 cm^{-1}. Consequently, a strong coupling between the plasmonic modes of gold nanorods and the mentioned vibrational frequencies is targeted, and thereby an approximate average wavenumber of 1650 cm^{-1} was taken as reference for our target calculation.

A schematic of the studied system is shown in Fig. S6. A canonical structure consisted of a square array with a lattice parameter W = 2.8 μm made up of identical gold nanorods with length L and a rectangular cross-section of sides 0.1 μm, 0.2 μm, 0.3 μm, and 0.4 μm with 70 nm height deposited on a CaF_2 substrate. Thereby, the signal response will be enhanced using an array of antennas, which multiplies the signal, despite the weak inter-antenna coupling for those separation distances. The optical response of bare AuNRs immersed in water as well as that of analogous AuNRs interacting with randomly distributed acrylamide molecules (AcMol) contained in a shell covering the AuNRA, (see schematics in Fig. 2a and description in Fig. S6) was determined following the methodology described in Section 4 of the SI. The dipole plasmon response of bare gold nanoantennas in water was characterized for different lengths and widths. The electromagnetic calculations show a blue shift in the spectral position of the plasmon resonances and a widening of the reflectivity curve as the cross-sectional area increases (Fig. S7). This analysis was expanded to the hybrid system comprised of AcMol and AuNRs, and particularly, the optical response of the nanoantennas was studied under variations of both acrylamide concentration and geometric dimensions.

To characterize the infrared response of the antenna-molecular

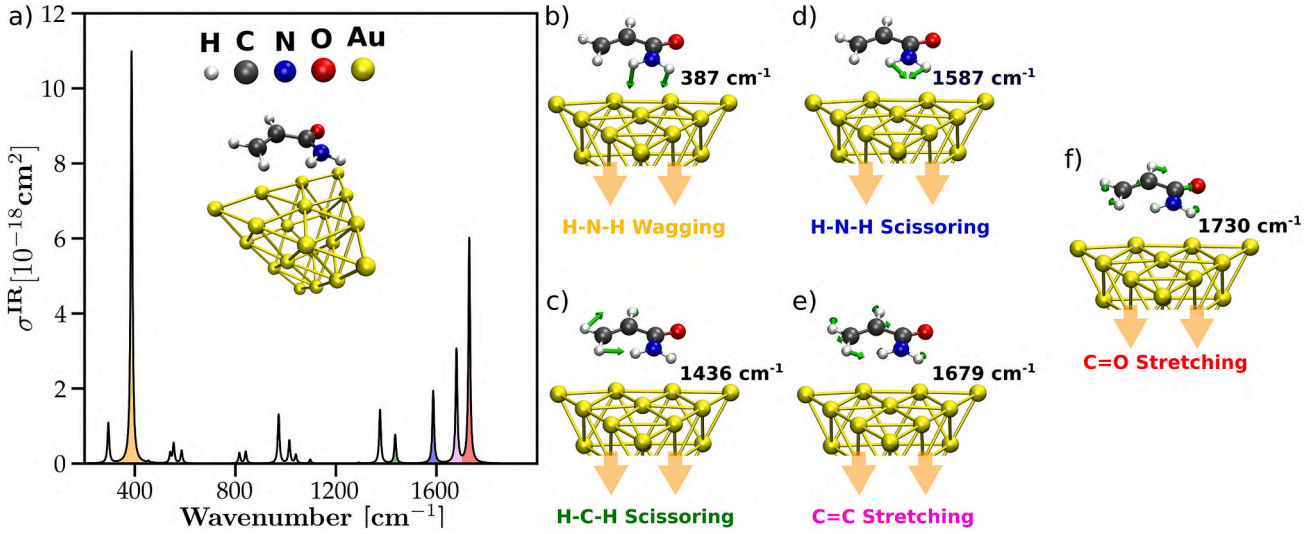

Fig. 1. Selected vibrational modes for Au_{20}-acrylamide: (a) Simulated IR absorption cross-section for Au_{20}-acrylamide in water as a function of the vibrational wavenumber between 200 cm^{-1} and 2000 cm^{-1}. The spectral lines are broadened by a Lorentzian function of width 8 cm^{-1}. The spectral lines of the selected vibrational modes H-N-H wagging, H-C-H scissoring, H-N-H scissoring, C═C stretching and C═O stretching are colored in orange, green, blue, violet, and red, respectively. The inset shows an atomistic model of the minimum energy structures for Au_{20}-acrylamide, where the white, grey, blue, red, and yellow spheres represent the atoms of hydrogen, carbon, nitrogen, oxygen, and gold, respectively. (b-f) Atomic displacements (green arrows) for five selected vibrational modes between 200 cm^{-1} and 2000 cm^{-1} for Au_{20} .acrylamide, along with the corresponding vibrational frequency in cm^{-1}. The orange arrows in panels b-f indicate that the gold cluster continues over that direction. For reference, the spectrum of the bare acrylamide in water is shown in Fig. S4. (For interpretation of the references to colour in this figure legend, the reader is referred to the web version of this article.)

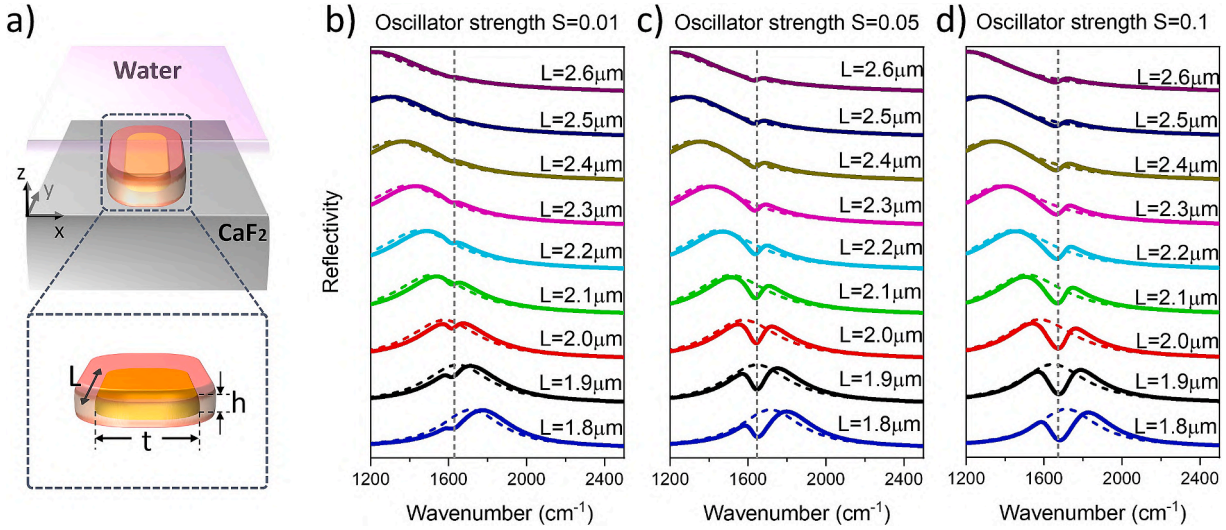

Fig. 2. Numerical comparison of the reflectivity of the bare gold nanorods (dashed lines) and that of the gold nanorods covered by a shell containing acrylamide molecules (AcMol) in water deposited on a CaF_2 substrate, and illuminated by a plane wave, with the electric field polarized along the main axis of the antennas (y-axis in the schematic representation in panel a)). The full-wave electromagnetic simulations use the dielectric functions of Au, CaF_2 and AcMol as described in the text. Panels b) c) and d) correspond to three different scenarios for the concentration of acrylamide, as described through the oscillator strength values S = 0.01 (b)), S = 0.05 (c)) and S = 0.1 (d)), for low, intermediate and large oscillator strength, respectively. The height (h) and width (t) of the antennas were fixed at 70 nm and 300 nm, respectively while the length (L) was varied between 1.8 μm and 2.6 μm. (For interpretation of the references to colour in this figure legend, the reader is referred to the web version of this article.)

hybrid system as the acrylamide concentration increases, the reflectivity of the system upon interaction with light was calculated in the infrared (IR) spectral range (specifically, from 4 μm to 8.5 μm wavelength, 2500 cm^{-1} to 1177 cm^{-1}). The results, shown in Fig. 2, correspond to three different scenarios depending on the concentration of acrylamide, as described by the Lorentz oscillator strength considered for defining its dielectric function (see Section 4 of the SI) for low (panel b)), intermediate (panel c) and large (panel d) molecular oscillator strength, S, respectively. The length of the nanoantennas was systematically varied from L = 1.8 μm to L = 2.6 μm in steps of 0.1 μm while the width and height was fixed at 300 nm and 70 nm, respectively for both the bare antenna system (dashed lines) and the coupled AuNRs-AcMol hybrid system (solid lines). The vertical dashed line at 1650 cm^{-1} represents approximately the mean value of the three largest vibrational cross sections frequencies for acrylamide.

The reflectivity spectrum of the bare nanoantennas in water, i. e., without acrylamide, shows a single broad plasmonic resonance that strongly depends on the length of the nanoantenna and corresponds to its longitudinal plasmonic mode. This dipolar plasmonic resonance shifts linearly with the antenna length for a fixed transverse cross section. On the other hand, the spectra of the hybrid nanoantennas-AcMol system show a modification of the spectral response, and a Fano-like profile is observed. This occurs because the plasmonic excitations are usually spectrally broad, and the characteristic narrow asymmetric Fano line-shape results upon interaction with the spectrally sharper acrylamide's vibrational modes. Because of this coupling, two peaks appear in this spectral area on both sides of the dip in the reflectivity spectra. These are split up as the oscillator strength S increases (from panel b to d, through c). The split of these peaks is caused by the coupling between the metal antenna plasmon and the vibrational excitation of the molecular acrylamide shell [9].

Two different regimes of interaction can be distinguished in Fig. 2. In panel b (low oscillator strength), the so-called weak coupling regime produces a slight dip in the reflectivity of the overall plasmonic resonance at the position of the vibration fingerprint. This dip can be used as a principle of molecular sensing, providing specificity due to the unambiguous identification of the molecule by its vibrational fingerprints. On the other hand, for strong coupling (panel d) a hybridization of the vibrations excited at the molecular layer and the plasmonic dipolar resonance produces new polaritonic modes, which are split spectrally in an upper (high energy), and lower (low energy) polariton branches respectively. The value of the spectral split of both polaritons can be used to retrieve the coupling strength and the oscillator strength of the AcMol.

The near-field distribution was studied for the bare antennas as well as for the antennas strongly coupled to the acrylamide molecule (large oscillator strength) for wavenumbers at 1560, 1650 and 1785 cm^{-1} in a water medium. Fig. 3 shows the simulations for antennas of 1.9 μm length and 300 nm width as described in Fig. 2a. Fig. 3a shows the reflectivity of the bare antenna (dashed line) and for the antennas coupled to the AcMol (solid line). The corresponding near-field distributions near the vibrational frequencies of AcMol are shown for situations without (Fig. 3b) and with acrylamide (Fig. 3c). The intensity of the spatially dependent near-field enhancement, which is mainly localized at a few nanometers distance from the antenna-tip ends, can reach up to 15 times the magnitude of the incoming field, as indicated in Fig. 3b. The near-field distribution in the middle panel of Fig. 3c illustrates how the coupled system shows less intense near-field at the AcMol vibrational resonance (dip in the corresponding far-field response) due to the coupling between the gold nanorods and the AcMol shell [28]. This effect can be understood as an induced transparency in which the strength of the phonon-polariton field plays a crucial role [9]. The localized plasmonic IR field shown in Fig. 3b and Fig. 3c can be used to enhance the spectral signature of acrylamide in this spectral range. Thus, the excitation of the phonon-polaritons in the AcMol shell on Au nanoantennas can induce coupling with the antenna plasmons, resulting in strong modifications of the plasmonic response.

To study the relevance of the antennas geometrical configuration in determining the antenna-molecule interaction regime, the coupling between the AuNRs and AcMol was studied for lateral thickness varying between 100 nm and 400 nm (Section 4 of the SI, Fig. S8).

3.3. Fabrication and qualitative characterization of bare gold nanorod antennas in air and deuterium oxide

The results of the IR response of the nanoantennas from the previous

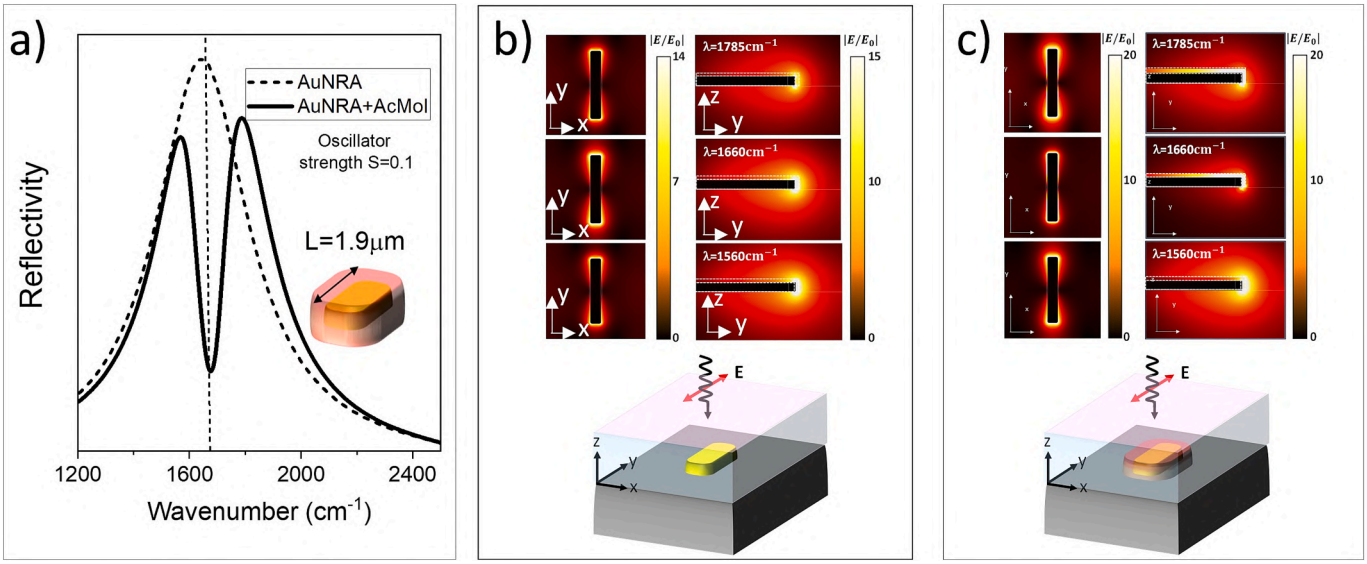

Fig. 3. a) Numerical comparison of the reflectivity between the bare AuNRAs (black, dashed line) and the AuNRAs covered by a shell containing acrylamide molecules (black, solid line) in water deposited on a CaF_2 substrate and illuminated by a plane wave, with the electric field polarized along the main axis of the nanorod, as described in the text. This spectrum is a selection from Fig. 2 for L = 1.9 μm and strong coupling. b) and c) Near-field distributions normalized to the electric field amplitude of the incident planewave at the frequencies of interest for the bare AuNRA and for the AuNRA coupled to the AcMol shell, respectively.

section provide a guide for fabrication of antennas that produce an optimal match with the selected acrylamide vibrational frequencies. With this purpose, three different gold nanorods, with lengths of 1.8 μm, 2.1 μm, and 2.4 μm, a lateral thickness of 300 nm, and a height of 70 nm were designed following a square symmetry with a 2.8 μm unit cell. The varying antenna lengths were patterned using electron beam lithography, followed by gold lift-off, and integrated into separate 1 × 1 mm arrays, as schematized in Fig. S2a. The entire area was encapsulated into a single microfluidic chip (Fig. S2b). Fig. S9 shows scanning electron microscopy (SEM) images of the fabricated gold nanorods.

The antenna arrays were characterized in air for the three selected lengths (Fig. S10). Their behavior shows a clear red shift of dipolar plasmon resonance around 300 cm^{-1} as the antenna length varies between 1.8 and 2.4 μm while the lower refractive index of air provokes a blue shift for the same length (as compared to water).

The gold nanoantennas were studied as immersed in deuterium oxide (D_2O) of 99.8 % purity in the isotope ^2H (as compared to the isotope ^1H) aiming to use the bare antennas as reference for posterior acrylamide solutions characterization. Fig. 4 shows the reflectance of the AuNRs with three different lengths all studied on the same microfluidic chip. A preliminary examination of the curves reveals that the far-field measurements align very well with the predictions from numerical calculations performed in a water environment showing a red shift of more than 300 cm^{-1} as the length varies from 1.8 μm to 2.4 μm. A detailed examination of the curves shows clear adsorption bands at 1200 cm^{-1}, 1450 cm^{-1} and 1650 cm^{-1}, which are related to the IR bending modes associated with the bonds D-O-D, H-O-D and H-O-H of the D_2O and H_2O molecules. Table S1 presents an overview of the IR vibration modes of D_2O and H_2O across the entire spectral range for easy identification [29]. The IR absorption for these bending modes is largely

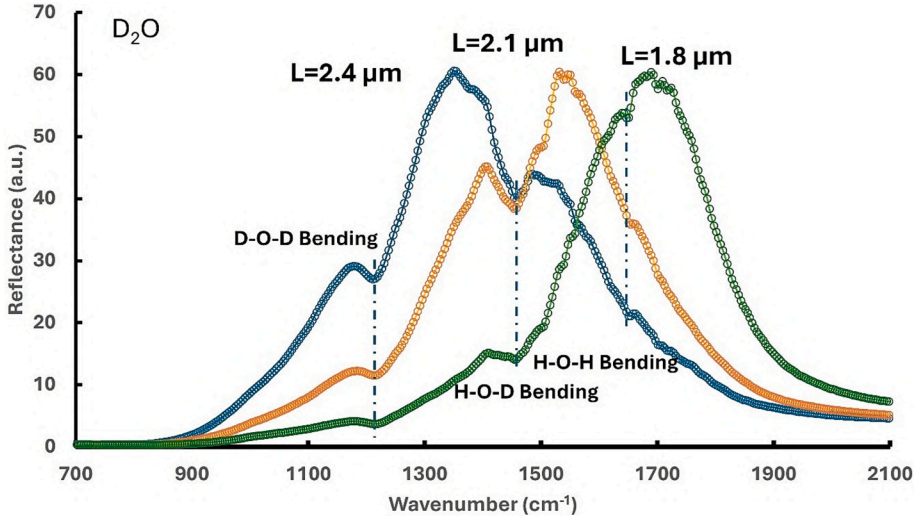

Fig. 4. FTIR spectroscopy characterization of gold nanorod antennas of different lengths in 99.8 % deuterium oxide. The respective lengths are indicated in the figure next to each curve (blue-L = 2.4 μm, orange-L = 2.1 μm, green-L = 1.8 μm). The different drops in the reflectance at specific wavenumbers correspond to light absorption due to D-O-D, H-O-D and H-O-H bending modes of D_2O and H_2O as described in the figure. (For interpretation of the references to colour in this figure legend, the reader is referred to the web version of this article.)

enhanced when the excited broad longitudinal dipolar plasmon of a particular antenna length spectrally matches the corresponding frequencies of these modes. This also provokes that the high absorption cross section of the asymmetric stretch of O—D around 2500 cm^{-1} is not visible in the whole measured spectral range (data not shown). Note that these spectral features associated with the vibrations of water were not included in the theoretical design of the nanoantenna (Section 3.2) for simplicity.

The presence of H-O-D and H-O-H bending modes can mask the peaks of the relevant IR vibrational modes of acrylamide. The presence of these modes can be justified because of the chemical equilibrium [30]:

$$H_2O + D_2O \leftrightarrow 2HDO\ K_{eq} = 3.86 \text{ at } 25^{\circ}C \quad (1)$$

At room temperature, and for an initial enrichment of water in the deuterium isotope of 99.8 %, the expected concentrations of species at equilibrium are 99.57 % of D_2O, 0.42 % of HDO and 5.10^{-4} % of H_2O, and thus this concentration allows for observing the fingerprint of the H-O-D and H-O-H bending modes (see Fig. S11).

3.4. Qualitative characterization of gold nanorod antennas in water-based acrylamide solutions

A 100 μg/ml acrylamide solution of 99.8 % D_2O was characterized by FTIR spectroscopy for the three antennas (Fig. 5). The first analysis of the reflectance spectrum reveals a strong absorption for the H-O-D bending mode of HDO and for the C═O stretching mode of acrylamide. The electrodynamical model calculations corroborate the experimental findings for the highest vibrational cross section mode above 1000 cm^{-1} (the C═O stretching for the acrylamide molecule). Therefore, for an antenna resonantly matching its plasmonic broadband resonance with the vibrational narrow band corresponding to C═O stretching (L = 1.8 μm), maximum contrast is obtained with a strong dip in the spectrum (green line in Fig. 5). This dip, which appears exactly at the vibrational frequencies [9] of the molecule, shows a characteristic Fano shape because there is not a perfect match between the plasmonic resonance and the C═O vibrational mode but a certain detuning of resonances leading to an asymmetric profile. As the length of the antennas is increased, the broadband plasmonic resonance is spectrally shifted to the red with respect to the selected molecular vibrational modes, producing a change in the phase interaction between the antenna resonance and the vibrational modes (modification of the coupling strength in terms of Fano interaction [31]), and progressively decreasing the intensity of the vibrational signals with emergence of clearly asymmetric profiles. These line shapes correspond to Fano-like profiles of detuned interaction [32]. The asymmetry of the line shapes is reversed when the broadband plasmonic resonance is red-or blue-detuned with respect to the spectral position of the molecular vibrations. For a completely detuned antenna respecting the C═O stretching mode (L = 2.1 μm and L = 2.4 μm), the asymmetric vibrational contrast is continuously reduced as observed in Fig. 5 (orange and blue lines respectively).

A closer observation of the reflectance for the 2.1 μm length antennas (inset in Fig. 5) shows the presence of small drops in the reflectance, denoting light absorption at 1500 cm^{-1}, 1550 cm^{-1} and 1565 cm^{-1}. These absorption bands can be associated with the H-C-H symmetric bending, H-N-H symmetric bending and C═C stretching bonds vibrations, respectively, which form the acrylamide vibrational fingerprints above 1300 cm^{-1}. The lower absorption of these modes, compared to that of the C═O stretching mode, may be attributed not only to the higher vibrational cross-section of the latter but also to the nearly perfect coupling achieved for C═O stretching mode at L = 1.8 μm as compared to that achieved for lower frequency modes at L = 2.1 μm. This coupling is a result of the energy match between the plasmonic and vibrational modes $\omega_{vib} \sim \omega_{plas}$.

Fig. 6 shows the reflectance curve for both the 10 μg/ml acrylamide solution and its solvent, the 99.8 % purity D_2O, when they are in proximity with the 1.8 μm length antennas array. The graph shows a strong absorption at approximately 1650 cm^{-1}, consequence of the almost perfect matching between the plasmonic resonance and the C═O stretching mode as well as the detuned H-O-D bending mode associated with the presence of HDO, which is totally detuned for this antenna length. A slight red shift in the plasmonic resonance, in response to the non-resonant high-frequency component of the refractive index of acrylamide, is observed. However, this shift is almost negligible for the same nanoantenna length, due to the relatively low difference in dielectric constant between acrylamide and water (compared to air). Therefore, baseline correction for curve comparison is not necessary.

Acrylamide solutions were also studied using higher purity D_2O solutions, with the aim of suppressing the strong absorption of the H-O-D bending mode in HOD. This approach was used to resolve the vibrational coupling of modes above 1000 cm^{-1} with the broad plasmonic resonance of the 2.1 μm length AuNRs. This strategy aims to reduce the HDO concentration at equilibrium (see Fig. S11) while examining the vibrational fingerprints of acrylamide at lower concentrations. Thus,

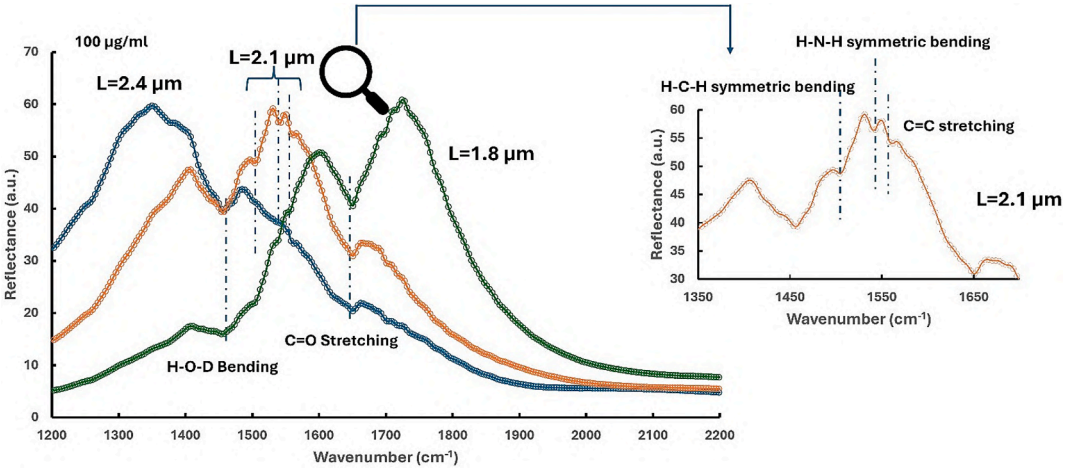

Fig. 5. FTIR spectroscopy characterization of different lengths of gold nanorod antennas in a 100 μg/ml acrylamide solution in a 99.8 % Deuterium Oxide solvent. The respective lengths are indicated in the figure next to each curve (L = 2.4 μm-blue, L = 2.1 μm-orange, L = 1.8 μm-green). The abrupt drops in the reflectance spectra corresponds to the H-O-D bending mode of HOD and the C═O stretching mode of acrylamide. The inset represents a zoom of the 1350–1700 cm^{-1} for the 2.1 μm length in which each absorption band is associated with different IR vibrations of the acrylamide molecule. (For interpretation of the references to colour in this figure legend, the reader is referred to the web version of this article.)

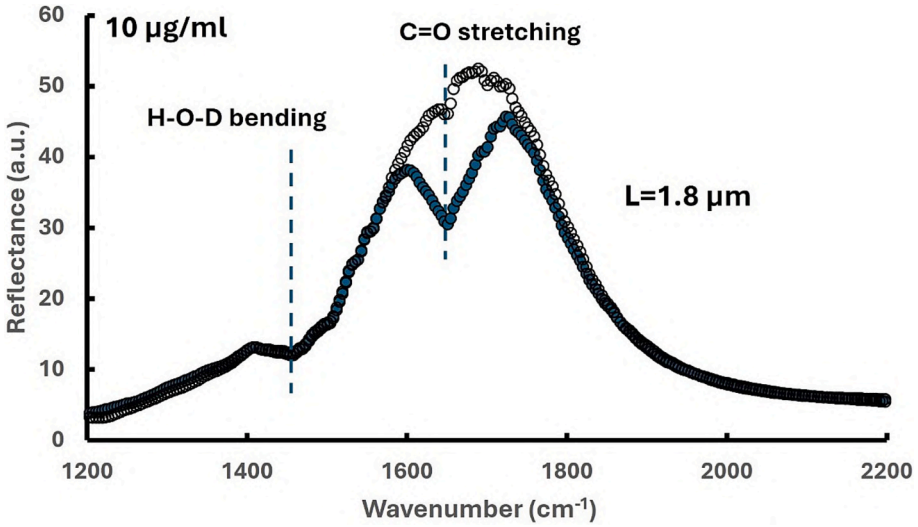

Fig. 6. Reflectance spectral curves for the 10 µg/ml acrylamide solution in 99.8 % purity Deuterium Oxide (blue circles) and Deuterium Oxide (white circles) for the 1.8 µm length gold nanorod arrays. The C═O stretching mode of the acrylamide and the H-O-D bending of D_2O are explicitly showed. (For interpretation of the references to colour in this figure legend, the reader is referred to the web version of this article.)

acrylamide was dissolved in 99.95 % pure D_2O. According to the equilibrium chemistry described in Eq. (1), this results in a theoretical molar concentration of 99.9 % D_2O, 0.099 % HDO, and 10^{-5} % H_2O.

Fig. 7 shows the obtained reflectance spectrum for 1 µg/ml acrylamide solution for both 1.8 µm and 2.1 µm lengths AuNRs, in which each antenna response in the same heavy water solvent without acrylamide is introduced for comparison. Fig. 7 highlights the nearly perfect match between the plasmonic resonance of the two antennas and the acrylamide's vibrational fingerprints in each respective spectral range. The 1.8 µm length antennas exhibit absorption of the C═O stretching mode, while the 2.1 µm length antennas show an almost complete suppression of the H-O-D bending mode of HDO and coupling with the acrylamide vibrational modes between 1500 cm^{-1} and 1600 cm^{-1}, labeled in Fig. 7 as lower frequency modes. Both curves show the vibrational fingerprint associated with the D-O-D bending of D_2O, but for nanoantennas of length 2.1 µm the spectral dip associated with this vibrational mode is more pronounced, due to the close proximity between the plasmonic resonance of the antenna and the vibrational frequency of this mode of the solvent.

Qualitative detection of acrylamide vibrational modes in the 1480 cm^{-1}-1580 cm^{-1} spectral range was performed by calculating the difference between the reflectance of 99.95 % purity heavy water and the reflectance of various acrylamide solutions with concentrations ranging from 500 ng/ml to 1 µg/ml. Fig. 8 shows this difference normalized to the heavy water reflectance for concentrations of 500 ng/ml and 1 µg/ml. The curve indicates changes in reflectance between 2 % and 5 % for the different vibrational modes in this spectral range. The relative maxima of the reflectance in this spectral range are located around 1568

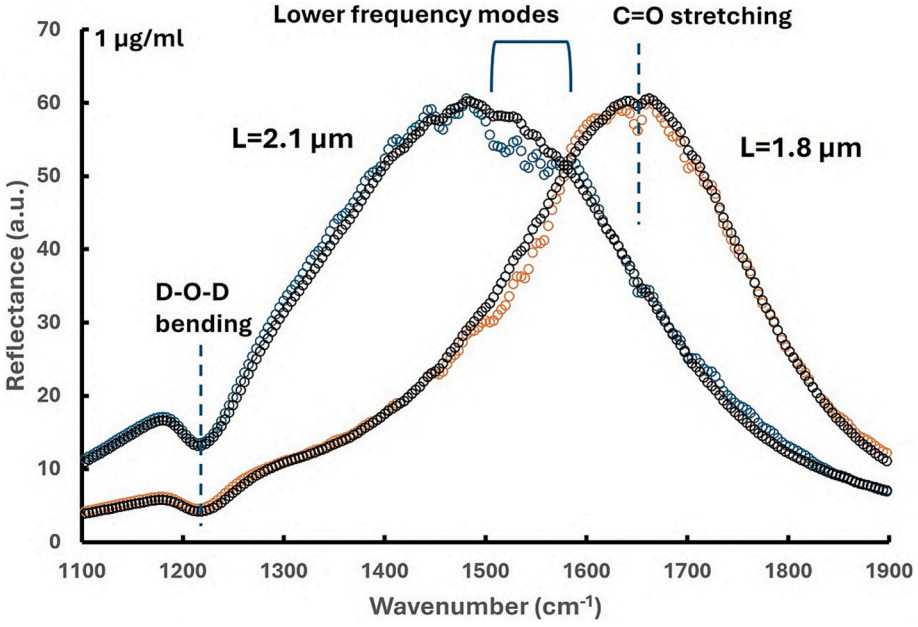

Fig. 7. Reflectance spectrum for 1 µg/ml of acrylamide solution in 99.95 % Deuterium Oxide for 1.8 and 2.1 µm lengths of gold nanorods arrays (L = 1.8 µm-orange circles, L = 2.1 µm-blue circles). The coupling between the antennas plasmonic responses, the acrylamide and heavy water vibrational modes can be clearly observed. The reflectance spectrum for Deuterium Oxide is also showed for comparison (black circles for both nanoantennas lengths). (For interpretation of the references to colour in this figure legend, the reader is referred to the web version of this article.)

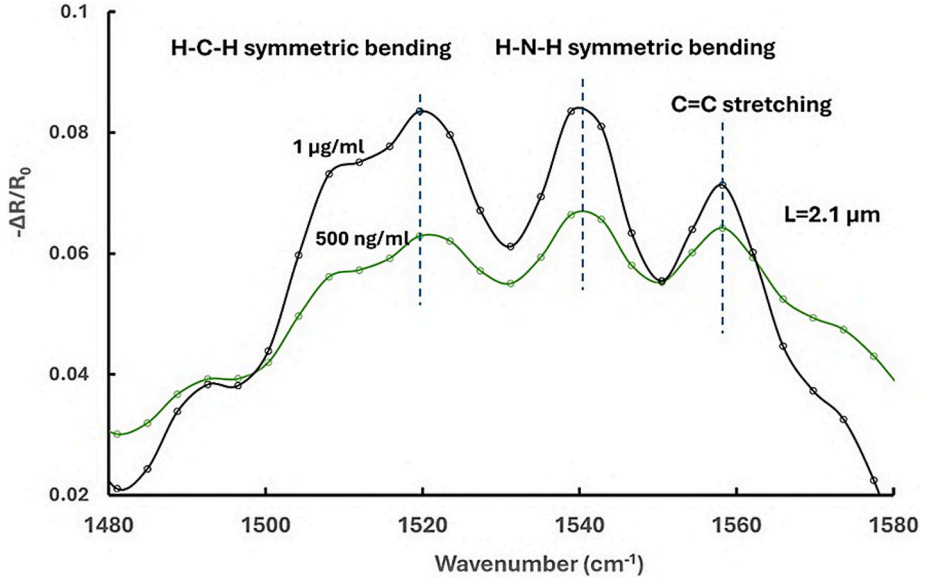

Fig. 8. Normalized reflectance difference spectrum between 99.95 % purity heavy water and different acrylamide concentrations: 500 ng/ml (green), and 1 µg/ml (black) for the 2.1 µm length antennas. Local maxima in this spectral range are attributed to H-C-H symmetric bending, H-N-H symmetric bending and C═C stretching. (For interpretation of the references to colour in this figure legend, the reader is referred to the web version of this article.)

cm^{-1}, 1535 cm^{-1} and 1515 cm^{-1} which denotes an acceptable correlation with C═C stretching, H-N-H symmetric bending and H-C-H symmetric bending modes as introduced in Fig. 8, and a reasonable agreement with the DFT results (1679 cm^{-1}, 1587 cm^{-1} and 1436 cm^{-1}, respectively, see Fig. 1). The difference between theoretical calculation and experimental data is reasonable considering the small model cluster used in DFT to simulate the absorption of the molecule-cluster system. More accurate models which account for anharmonic effects and the local environment of the molecule, including larger clusters and intermolecular interactions, may also influence the SEIRA signal. Modelling these effects is challenging for tractable DFT simulations.

To validate the vibrational fingerprints obtained by SEIRA and DFT calculations, conventional FTIR spectroscopy and ATR were used (Section 6 of Supplementary Data) to validate the acrylamide's vibrational modes as different concentrations of acrylamide (100 µg/ml, 1200 µg/ml and 5000 µg/ml) in high purity heavy water.

In the ATR analysis (Fig. S12), nearly identical spectra were obtained for heavy water alone and for acrylamide solutions at concentrations of 100 and 1200 µg/ml. The C═O and C═C stretching modes of acrylamide are only faintly visible for the 5000 µg/ml at 1659 and 1600 cm^{-1}, respectively. The spectra also show a strong absorption band at 1205 cm^{-1}, attributed to the D–O–D bending vibration of heavy water, as well as a broad absorption centered around 2500 cm^{-1}, corresponding to the symmetric and asymmetric D—O stretching modes.

In the FTIR spectroscopy analysis (Fig. S13), nearly identical spectra were obtained for dried heavy water alone and for dried acrylamide solutions at concentrations of 100 and 1200 µg/ml. For a 5000 µg/ml, the vibrational modes are observed at 1650 cm^{-1} (C═O stretching), 1605 cm^{-1} (C═C stretching), 1460 cm^{-1} (H-NH scissoring) and at 1385 cm^{-1} (H-C-H scissoring). These data demonstrate that SEIRA spectroscopy significantly enhances vibrational infrared absorption by coupling molecular signals to the plasmonic response of gold nanoresonators. Additionally, the observed vibrational frequencies show good agreement between SEIRA spectroscopy and DFT calculations.

3.5. Quantitative detection of acrylamide

To study the limit of detection of the SEIRA-based sensor, acrylamide solutions were injected into the microfluidic chip at increasing concentrations. According to the previous results, the antenna length was set at 1.8 µm to study the strong C═O absorption and the resonant plasmonic response while the acrylamide absorbance signal was calculated as $A = -10^3 * \log_{10}(R_{acrylamide}/R_0)$ where $R_{acrylamide}$ represents the reflectance at the different acrylamide concentrations and R_0 the reflectance for the D_2O solution.

Thus, it was possible to establish a dependence of the C═O vibrational peak intensity as a function of acrylamide concentrations as follows. In Fig. 9 the integrated band absorbance for the C═O stretching mode for different acrylamide concentrations is shown, with the inset displaying a zoomed linear plot for the lowest concentrations ranging from 500 ng/ml to 1 µg/ml. Fig. S14 describes the absorption peak, at 1650 cm^{-1}, corresponding to the C═O stretching mode. Both curves are studied because the SEIRA signals at low and high concentration ranges reflect dissimilar profiles because of the dip amplitude in the reflectivity and that the two peaks in both sides of the dip split up as the acrylamide concentration increases. This broad concentration range changes the line shape of SEIRA signals, hampering accurate readout of the target vibrational frequency and spectral intensity for quantitative analysis. In fact, for higher acrylamide concentrations, a hybridization of the vibrations excited at the molecular layer and the plasmonic dipolar resonance produces new polaritonic modes, which are split spectrally in an upper (high energy) and lower (low energy) polariton branches respectively [33] as can be also seen in the simulations showed in the Fig. 2c. The change in the line shape of the SEIRA signal complicates the calculation of the integrated absorbance band due to the dependence of the band width on concentration (Fig. S15). Therefore, when studying significantly different concentrations or electromagnetic field enhancements, the absorbance at the vibration peak [34] or the SEIRA signal contrast [35], represented as a difference between the maximum and minimum of the baseline corrected, are respectively represented instead.

The obtained s-shape for the C═O stretching band absorbance covers a large concentration range from 500 ng/ml to 100 µg/ml and the sigmoidal shape of the curves fits well with a Langmuir isothermal model [36]. The absorbance signal from an injection of 400 ng/ml is slightly lower than three times the absorbance signal obtained from acrylamide-devoid heavy water (negative control). Therefore, we can infer that the lower limit of detection is around 500 ng/ml.

The absorbance is strongly influenced by acrylamide molecules adsorbed onto gold, particularly at the tips of the antennas. The number of molecules adsorbed on the plasmonic surface and contributing to the

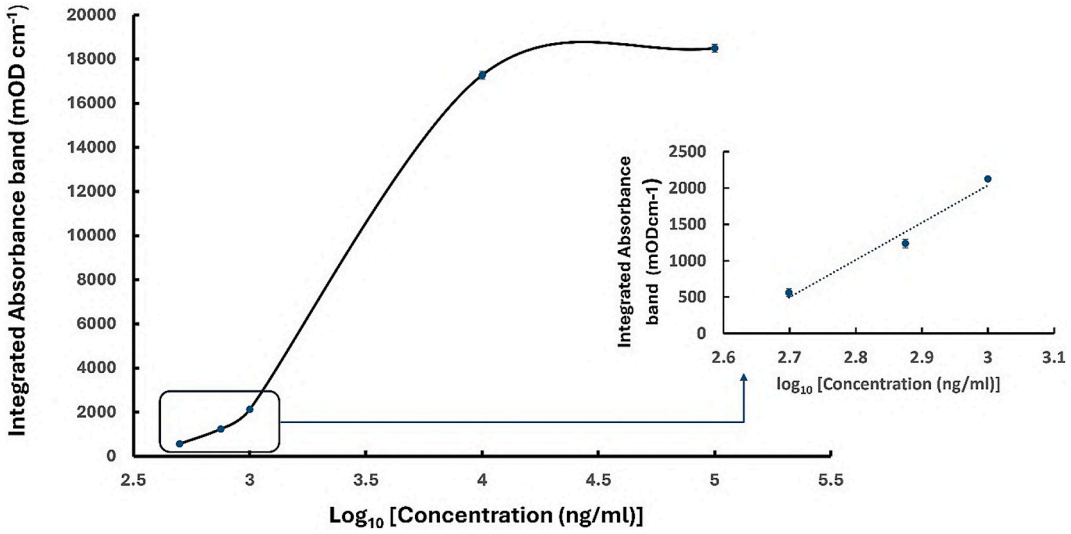

Fig. 9. Integrated absorbance band for the C═O stretching mode. A linear fit is displayed in the inset for the low concentration range.

enhanced signal depends on the surface concentration of the acrylamide adsorbate, the metallic surface area, the density of metallic structures, and the area of the excitation due to the incident radiation. Acrylamide forms a multilayer homogeneous adsorption in which van der Waals forces are the main contribution to the physical adsorption. This adsorption can be described by the Brunauer, Emmett, and Teller (BET) isothermal [36], which neglects physical interaction between adsorbed molecules. This isotherm converges to a Langmuir isotherm as the molecules adsorbed on the surface form a monolayer [37]. Therefore, the Langmuir-like behavior observed in acrylamide adsorption suggests that the primary contribution to absorption comes from the molecules directly adsorbed on top of the antennas. This can be explained by the fact that the electric field surface enhancement decays within a few nanometers from the surface, making it ideally suited to collect information primarily from the molecular layer in direct contact with the antennas.

4. Conclusions

An appropriate design of IR nanoantennas has been shown to be key to enhance specific molecular fingerprints from acrylamide molecular layers, enhancing substantially the detection limits of this substance. To implement a rational design, DFT was applied to calculate the infrared absorption spectrum of the acrylamide molecule in a water solution, including the effect of the chemical environment of the nanoantenna gold atoms in the IR absorption cross section of the molecules. From the spectral information of the main fingerprints of acrylamide on gold, numerical full electromagnetic calculations were developed in a water optical medium to determine the dimensions of gold nanoantennas that produce a match of their plasmon resonances with the highest infrared vibrational modes of acrylamide above 1000 cm^{-1}. The SEIRA signal characterization showed efficient coupling between the antennas' resonances and the target acrylamide frequencies as the antenna length is varied for tuning its plasmon resonance.

The integration of different antenna lengths under the same substrate provides efficient coupling with acrylamide infrared vibrational modes at different spectral ranges, providing a solution for acrylamide recognition without the use of specific receptors or labels. The differences between calculated and experimental results may arise from several factors, including the choice of the model cluster, the basis set in DFT calculations, anharmonic effects, the experimental conditions of the acrylamide solutions, as well as instrumental effects like the response function and resolution, and potential experimental artifacts. Despite these discrepancies, it is important to point out that the DFT-calculated spectrum exhibits a one-to-one correspondence with the SEIRA characterization.

Simple SEIRA signal analysis of the strongest vibrational fingerprint of acrylamide above 1000 cm^{-1} enables its detection at concentrations as low as 500 ng/ml whereas conventional FTIR spectroscopy can only detect it at concentrations around 5000 μg/ml. This level of sensitivity is comparable to that achieved by antibody-based immunoassays in spiked food samples [38]. However, SEIRA offers the advantage of operating without the need for recognition or labeled molecules.

One of the main drawbacks of applying SEIRA in the food industry is the potential interference from other compounds, which makes spectral analysis more difficult. Food products such as coffee, biscuits, and toasted bread contain a variety of molecules, including organic acids, carbohydrates, lipids, and proteins that contribute significantly to their vibrational spectra. For example, proteins primarily influence the Amide I and Amide II spectral regions (1550–1650 cm^{-1}), while lipids show strong absorption bands in the 2800–3000 cm^{-1} range. Therefore, minimal sample preparation is typically required, involving the use of organic solvents to extract lipids and deproteinizing agents to remove proteins [39]. In food products that are potentially rich in acrylamide such as coffee and fried potatoes various components like proteins, lipids, Maillard reaction products, carbohydrates, and caffeine are present in one or both matrices, resulting in absorption within the same spectral regions as acrylamide. For instance, during the heating of fried potatoes, oxidized lipids are formed, producing carbonyl groups and esters that absorb near 1700 cm^{-1}. In roasted coffee, melanoidins—one of its main components—exhibit strong absorption around 1550 cm^{-1}. To avoid these interferences, pre-treatment techniques such as solid-phase extraction to isolate and concentrate acrylamide while removing interfering compounds is necessary before SEIRA spectroscopy. Another approach is to integrate different plasmonic resonators—each with slight variations in their critical dimensions—onto the same substrate. It allows the separation and selective enhancement of both high- and low-energy vibrational fingerprints associated with acrylamide. To further improve the detection accuracy, this strategy could be complemented with multivariate data analysis based on chemometrics methods.

For a practical use of SEIRA spectroscopy in complex food matrices, it could be complemented by Explainable Artificial Intelligence (XAI), an approach that based on the physical phenomenon of coupling between the electromagnetic response of the antenna and the characteristic vibrational frequencies of the more abundant molecules in the sample, can predict the presence or concentration of acrylamide from SEIRA spectra applying Machine Learning algorithms. Combining SEIRA

signals with XAI approaches will enable the development of transparent, predictive models that move beyond the current 'black box' trend, offering well-founded interpretations of the relationship between spectral features and molecular composition. It will support the development of sensitive, label-free optical spectroscopic sensors. Finally, this strategy could significantly surpass those solutions based solely on data analysis, which might introduce artifacts related to the discrete nature of the data sets and are not easily adaptable to experimental changes, such as the use of different food matrices or different spectroscopic setups.

Declaration of competing interest

The authors declare that they have no known competing financial interests or personal relationships that could have appeared to influence the work reported in this paper.

Acknowledgements

This work has been partially funded by the Basque Government under the research project ELKARTEK KK-2022/00041 and the Gipuzkoa Quantum program's 2022 call under the research project QUANTUM SEIRA (2022-QUAN-000034-01).

RAB, MZH and JA acknowledge funding from the project IT1526-22 of the Basque Government for consolidated groups of the University of the Basque Country, and project PID 2022-139579NB-I00 (QueVEDO) of Spanish Ministry of Science and Technology. RAB and MZH acknowledge the financial support from the grant awarded to the QSEIRA project (2024-QUAN-000011-01) from the Gipuzkoa Quantum program's 2024 call of the Department of Economic Promotion and Strategic Projects of the Provincial Council of Gipuzkoa. RAB and MHZ are thankful for the technical and human support provided by the Donostia International Physics Center (DIPC) Computer Center.

Appendix A. Supplementary data

Supplementary data to this article can be found online at https://doi.org/10.1016/j.saa.2025.126772.

Data availability

The data that support the findings of this study are available within the article and its supplementary material.

References

[1] Acrylamide EFSA (europa.eu).
[2] European Food Safety Authority (EFSA), Diane Benford, Margherita Bignami, James Kevin Chipman, Luisa Ramos Bordajandi, Assessment of the genotoxicity of acrylamide, EFSA J. 20 (5) (2022) 7293, https://doi.org/10.2903/j.efsa.2022.7293.
[3] Commission Regulation (EU) 2017/2158. Regulation - 2017/2158 - EN - EUR-Lex (europa.eu).
[4] Commision Regulation (EU) 2019/1888. EUR-Lex - 32019H1888 - EN - EUR-Lex (europa.eu).
[5] Wu Jing, Y. Dong Shen, Hong-Tao Lei, Yunag-Ming Sun, Jin-Yi Yang, Zhi-Li Xiao, Hong Wang, Zhen-Lin Xu, Hapten synthesis and development of a competitive indirect enzyme-linked immunosorbent assay for acrylamide in food samples, J. Agric. Food Chem. 62 (29) (2014) 7078–7084, https://doi.org/10.1021/jf5015395.
[6] Yuting Zhu, Shanshan Song, Liquiang Liu, Hua Kuang, Chuanlai Xa, An indirect competitive enzyme-linked immunosorbent assay for acrylamide detection based on a monoclonal antibody, Food Agric. Immunol. 27 (2016) 6, https://doi.org/10.1080/09540105.2016.1160369.
[7] Wu Min-Fu, Yu Wang, Sha Li, Xiu-Xiu Dong, Jin-Yi Yang, Yu-Dong Shen, Hong Wang, Yuan-Ming Sun, Hong-Tao Lei, X. Zhen-Lin, Ultrasensitive immunosensor for acrylamide based on chitosan/SnO2-SiC hollow sphere nanochains/gold nanomaterial as signal amplification, Anal. Chim. Acta 1049 (2019) 188–195, https://doi.org/10.1016/j.aca.2018.10.041.
[8] Lin Luo, Bao-Zhu Jia, Xiao-Qun Wei, Zhi-Li Xiao, Hong Wang, Yuan-Ming Sun, Yu-Dong Shen, Hong-Tao Lei, Xu. Zhen-Lin, Development of an inner filter effect-based fluorescence immunoassay for the detection of acrylamide using 9-xanthydrol, Sensors Actuators B 332 (2021) 129561, https://doi.org/10.1016/j.snb.2021.129561.
[9] Frank Neubrech, Annemarie Pucci, Thomas Walter Cornelius, Shafqat Karim, Aitzol García-Etxarri, Javier Aizpurua, Resonant Plasmonic and vibrational coupling in a tailored Nanoantenna for infrared detection, Phys. Rev. Lett. 101 (15) (2008) 157403–157406, https://doi.org/10.1103/PhysRevLett.101.157403.
[10] Aurelian John-Herpin, Andreas Tittl, Lucca Kühner, Felix Richter, Steven H. Huang, Gennady Shvets, Oh. Sang-Hyun, Hatice Altug, Metasurface-enhanced infrared spectroscopy: an abundance of materials and functionalities, Adv. Mater. 35 (2023) 2110163, https://doi.org/10.1002/adma.202110163.
[11] Jikai Wang, Pengfei Zeng, Xilin Xiao, Cheng Zhou, Hua Wei, Yu. Cuiyun, Recent advances in nanostructured substrates for surface-enhanced infrared absorption spectroscopy, Nanotechnology 34 (38) (2023) 382002, https://doi.org/10.1088/1361-6528/acd943.
[12] Axel D. Becke, A new mixing of Hartree–Fock and local density-functional theories, J. Chem. Phys. 98 (1993) 1372–1377, https://doi.org/10.1063/1.464304.
[13] Johannes Neugebauer, Bernd A. Hess, Fundamental vibrational frequencies of small polyatomic molecules from density-functional calculations and vibrational perturbation theory, J. Chem. Phys. 118 (16) (2003) 7215–7225, https://doi.org/10.1063/1.1561045.
[14] Said Daoui, Cemile Baydere, Feride Akman, Fouad El Kalai, Lhassane Mahi, Necmi Dege, Yildiray Topcu, Khalid Karrouchi, Noureddine Benchat, Synthesis, X-ray crystallography, vibrational spectroscopy, thermal and DFT studies of (E)-6-(4-methylstyryl)-4,5-dihydropyridazin-3(2H)-one, J. Mol. Struct. 1225 (2021) 129180, https://doi.org/10.1016/j.molstruc.2020.129180.
[15] Sevgi Kansiz, Mohammad Azam, Taskin Basili, Seher Meral, Feyzi Alkim Aktas, Semanur Yesilbag, Kim Min, Aysen Alaman Agar, Necmi Dege, synthesis, structural studies, Hirshfeld surface analysis, and molecular docking studies of a thiophene-based Schiff base compound, J. Mol. Struct. 1265 (2022) 133477, https://doi.org/10.1016/j.molstruc.2022.133477.
[16] Florian Weigend, Reinhart Ahlrichs, Balanced basis sets of split valence, triple zeta valence and quadruple zeta valence quality for H to Rn: design and assessment of accuracy, Phys. Chem. Chem. Phys. 7 (2005) 3297–3305, https://doi.org/10.1039/B508541A.
[17] S. Miertuš, E. Scrocco, J. Tomasi, Electrostatic interaction of a solute with a continuum. A direct utilization of AB initio molecular potentials for the prevision of solvent effects, Chem. Phys. 55 (1) (1981) 117–129, https://doi.org/10.1016/0301-0104(81)85090-2.
[18] P. Jeffrey Hay, Willard R. Wadt, *Ab initio* effective core potentials for molecular calculations. Potentials for K to Au including the outermost core orbitals. P.J. Hay et al, J. Chem. Phys. 82 (1985) 299–310, https://doi.org/10.1063/1.448975.
[19] Stefan Grimme, Jens Antony, Stephan Ehrlich, Helge Krieg, A consistent and accurate ab initio parametrization of density functional dispersion correction (DFT-D) for the 94 elements H-Pu. S. Grimme et al, J. Chem. Phys. 132 (2010) 154104, https://doi.org/10.1063/1.3382344.
[20] Stefan Grimme, Stephan Ehrlich, Lars Goerigk, Effect of the damping function in dispersion corrected density functional theory, J. Comput. Chem. 32 (2011) 1456–1465, https://doi.org/10.1002/jcc.21759.
[21] M.J. Frisch, G.W. Trucks, H.B. Schlegel, G.E. Scuseria, M.A. Robb, J.R. Cheeseman, G. Scalmani, V. Barone, G.A. Petersson, H. Nakatsuji, X. Li, M. Caricato, A. V. Marenich, J. Bloino, B.G. Janesko, R. Gomperts, B. Mennucci, H.P. Hratchian, J. V. Ortiz, A.F. Izmaylov, J.L. Sonnenberg, D. Williams Young, F. Ding, F. Lipparini, F. Egidi, J. Goings, B. Peng, A. Petrone, T. Henderson, D. Ranasinghe, V. G. Zakrzewski, J. Gao, N. Rega, G. Zheng, W. Liang, M. Hada, M. Ehara, K. Toyota, R. Fukuda, J. Hasegawa, M. Ishida, T. Nakajima, Y. Honda, O. Kitao, H. Nakai, T. Vreven, K. Throssell, J.A. Montgomery Jr., J.E. Peralta, F. Ogliaro, M. J. Bearpark, J.J. Heyd, E.N. Brothers, K.N. Kudin, V.N. Staroverov, T.A. Keith, R. Kobayashi, J. Normand, K. Raghavachari, A.P. Rendell, J.C. Burant, S.S. Iyengar, J. Tomasi, M. Cossi, J.M. Millam, M. Klene, C. Adamo, R. Cammi, J.W. Ochterski, R.L. Martin, K. Morokuma, O. Farkas, J.B. Foresman, D.J. Fox, Gaussian 16, Revision C.01, Gaussian, Inc., Wallingford CT, 2016. Citation | Gaussian.com.
[22] COMSOL, COMSOL Multiphysics v5.2, AB, Stockholm, Sweden. http://www.comsol.com.
[23] D. Rodrigo, A. Tittl, N. Ait-Bouziad, A. John-Herpin, O. Limaj, C. Kelly, D. Yoo, N. J. Wittenberg, S.H. Oh, H.A. Lashuel, H. Altug, Resolving molecule-specific information in dynamic lipid membrane processes with multi-resonant infrared metasurfaces, Nat. Commun. 9 (2018) 2160, https://doi.org/10.1038/s41467-018-04594-x.
[24] N. Jonathan, The infrared and Raman spectra and structure of acrylamide, J. Mol. Spectrosc. 6 (1961) 205–214, https://doi.org/10.1016/0022-2852(61)90243-0.
[25] N. Sundaraganesan, N. Puviarasan, S. Mohan, Vibrational spectra, assignments and normal coordinate calculation of acrylamide, Talanta 54 (2001) 233–241, https://doi.org/10.1016/S0039-9140(00)00585-3.
[26] Yoon Hyuck Kim, Jaw-Seung Lee, Acrylamide: new organic solvent with chemically tunable viscosity for rapid gram-scale synthesis of gold nanoparticles, ACS Omega 7 (2022) 45277–45286, https://doi.org/10.1021/acsomega.2c05813.
[27] K.B. Girma, V. Lorenz, S. Blaurock, F.T. Edelmann, Coordination chemistry of acrylamide, Coord. Chem. Rev. 249 (2005) 1283–1293, https://doi.org/10.1016/j.ccr.2005.01.028.
[28] Christian Huck, Jochen Vogt, Neuman Tomáš, Tadaaki Nagao, Reiner Hillenbrand, Javier Aizpurua, Annemarie Pucci, Frank Neubrech, Strong coupling between phonon-polaritons and plasmonic nanorods, Opt. Express 24 (22) (2016) 25528, https://doi.org/10.1364/OE.24.025528.
[29] Kyueun Park, Youngjin Kim, Kyung Jin Lee, Analysis of deuterated water contents using FTIR bending motion, J. Radioanal. Nucl. Chem. 322 (2019) 487–493, https://doi.org/10.1007/s10967-019-06734-z.

[30] J.G. Bayly, V.B. Kartha, W.H. Stevens, The absorption spectra of liquid phase H_2O, HDO and D_2O from 0.7 μm to 10 μm, Infrared Phys. 3 (4) (1963) 211–222, https://doi.org/10.1016/0020-0891(63)90026-5.
[31] Javier Aizpurua, F. Thomas Taubner, Javier García, Markus Brehm de Abajo, Rainer Hillenbrand, Substrate-enhanced infrared near-field spectroscopy, Opt. Express 16 (2008) 1529–1545, https://doi.org/10.1364/OE.16.001529.
[32] U. Fano, Effects of configuration interaction on intensities and phase shifts, Phys. Rev. 124 (1981) 1866, https://doi.org/10.1103/PhysRev.124.1866.
[33] Shunping Zhang, Xu. Hongxing, Understanding the lineshape of surface-enhanced infrared absorption spectra, Natl. Sci. Rev. 8 (2021) 4, https://doi.org/10.1093/nsr/nwaa240.
[34] Aurelian John-Herpin, Andreas Tittl, Hatice Altug, Quantifying the limits of detection of surface-enhanced infrared spectroscopy with grating order-coupled nanogap antennas, ACS Photonics 5 (10) (2018) 4117–4124, https://doi.org/10.1021/acsphotonics.8b00847.
[35] Tomás Neuman, Christian Huck, Jochen Vogt, Frank Neubrech, Rainer Hillenbrand, Javier Aizpurua, Annemarie Pucci, Importance of plasmonic scattering for an optimal enhancement of vibrational absorption in SEIRA with linear metallic antennas, J. Phys. Chem. C 119 (2015) 26652, https://doi.org/10.1021/acs.jpcc.5b08344.
[36] Mahdieh Mozaffari Majd, Vahid Kordzadeh-Kermani, Vahab Ghalandari, Anis Askari, Mika Sillanpaa, Adsorption isothermal models: a comprehensive and systematic review (2010−2020), Sci. Total Environ. 812 (2022) 151334, https://doi.org/10.1016/j.scitotenv.2021.151334.
[37] Jianlong Wang, Xuan Guo, Adsorption isotherm models: classification, physical meaning, application and solving method, Chemosphere 258 (2020) 127279, https://doi.org/10.1016/j.chemosphere.2020.127279.
[38] Yifan Liang, Yuyao Zeng, Lin Luo, Xu Zhenlin, Yudong Shen, Hong Wang, Bruce D. Hammock, Detection of acrylamide in foodstuffs by nanobody-based immunoassays, J. Agric. Food Chem. 70 (29) (2022) 9179–9186, https://doi.org/10.1021/acs.jafc.2c01872.
[39] Yuchen Zhu, Yinghua Luo, Guoyu Sun, Pengpu Wang, Hu Xiaosong, Fang Chen, Inhibition of acrylamide by glutathione in asparagine/glucose model systems and cookies, Food Chem. 329 (2020) 127171, https://doi.org/10.1016/j.foodchem.2020.127171.